ACS APPLIED ENERGY MATERIALS

www.acsaem.org Article

A Layered $Zn_{0.4}VOPO_4{\cdot}0.8H_2O$ Cathode for Robust and Stable Zn Ion Storage

Zeyi Wu, Yanan Wang, Lin Zhang, Le Jiang, Wenchao Tian, Cailing Cai, Jason Price, Qinfen Gu, and Linfeng Hu*

Cite This: *ACS Appl. Energy Mater.* 2020, 3, 3919−3927 Read Online

ACCESS | Metrics & More | Article Recommendations | Supporting Information

ABSTRACT: Rechargeable aqueous zinc-ion batteries (ZIBs) have shown extraordinary potential in recent years due to their prominent superiority including resource sustainability, nontoxicity, excellent energy density of the zinc anode, and better safety. Nevertheless, the development of ZIBs is still hindered by the lack of suitable cathode materials possessing a high discharge voltage, sufficient specific energy density, and long-term cycle life. Herein, our work reported a layered phosphate, $Zn_{0.4}VOPO_4{\cdot}0.8H_2O$, by topochemical incorporation of zinc ions into the $VOPO_4{\cdot}2H_2O$ framework. The incorporation of zinc ions makes no change in the in-plane atomic arrangement and coordination environment. The resulting $Zn_{0.4}VOPO_4{\cdot}0.8H_2O$ depicted a specific capacity of 161.4 $mAh{\cdot}g^{-1}$, a discharge plateau of 1.45 V, and excellent cycling stability over 1000 cycles. The energy density of our $Zn//Zn_{0.4}VOPO_4{\cdot}0.8H_2O$ battery was as high as 219.8 $Wh{\cdot}kg^{-1}$ at a power density of 136.2 $W{\cdot}kg^{-1}$. A typical zinc ion intercalation/deintercalation mechanism has been revealed in this layered cathode. This work provides a layered hydrated phosphate as a robust cathode for ZIBs and also sheds light on modulation of multivalent-ion storage performance by a topochemical strategy in layered materials.

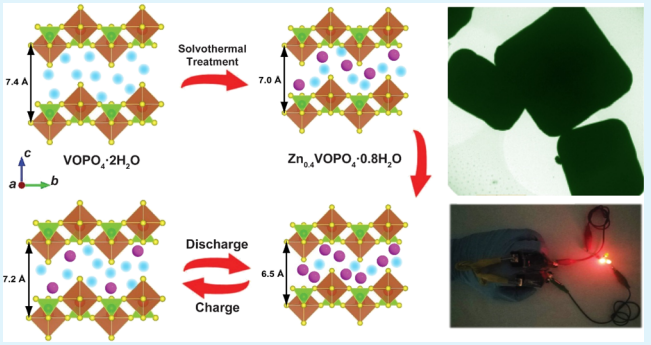

KEYWORDS: *topochemistry, layered compounds, $Zn_{0.4}VOPO_4{\cdot}0.8H_2O$, intercalation/deintercalation, zinc-ion secondary battery*

1. INTRODUCTION

As one of the most popular energy storage devices, secondary zinc-ion batteries (ZIBs) have shown extraordinary development potential in recent years due to their prominent superiority including relative resource sustainability (abundant zinc resource reserve), better safety, environment friendliness (aqueous-based electrolytes), and excellent volumetric energy density (nearly 5855 $mAh{\cdot}cm^{-3}$ compared to 2061 $mAh{\cdot}cm^{-3}$ for lithium-ion batteries).[1−4] Nevertheless, the development of ZIBs is still hindered by the lack of suitable cathode materials possessing sufficient specific energy density and long-term cycle life. Up to date, the most commonly studied cathodes are Mn-based and V-based oxides. Mn-based oxides show high specific capacity due to their remarkable diversity of crystal structure and unique tunnel structure for facile zinc ion transport.[2−14] However, Mn-based oxides generally suffer from Mn^{2+} dissolution and poor cycling stability caused by the Jahn−Teller effect.[2,5] On the other hand, V-based oxides exhibit longer cycle lives and higher rate performances, but their low discharge voltage around 0.6−0.8 V significantly limits the energy density of the battery.[8−10] Thus, the development on cathode materials that combine both high discharge voltage and excellent cycling stability is highly desired and also very challenging.

Layered phosphate compounds have attracted considerable research interests on ZIBs owing to their unique layered structure and enriched electrochemical activity.[15−18] Among them, layered hydrated phosphate ($VOPO_4{\cdot}2H_2O$) is a bilayer structure where the adjacent layers are held together by weak bonding interactions with the characteristic of corner-shared VO_6 octahedra linking to PO_4 tetrahedra as a host layer,[19,20] and it has been already reported as a promising cathode material for pseudocapacitors,[21] Li^+,[19] Na^+,[22] and Mg^{2+}[23] secondary batteries. Most recently, it has been reported that $VOPO_4$ could be utilized as a Zn^{2+} intercalation host cathode of aqueous ZIBs, taking advantage of the rich chemical valence states of V (V^{5+}, V^{4+}, and V^{3+}) and the open interlayer spacing (7.43 Å) of the two-dimensional (2D) structure.[16−18]

Recent advances demonstrated that modulating the interlayer structure by employing intercalated polymer molecules or metal cations could significantly boost the

Received: February 14, 2020
Accepted: April 1, 2020
Published: April 1, 2020

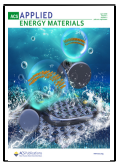

https://dx.doi.org/10.1021/acsaem.0c00318
ACS Appl. Energy Mater. 2020, 3, 3919−3927

capacity and cycle performance of the cathode. For instance, Wang et al. designed and fabricated a polyaniline-intercalated MnO_2 that served as the cathode of aqueous ZIBs, which showed excellent long-term stability of 5000 cycles at a utilization of 40% of the theoretical capacity.[24] This emerging report inspires us to consider the following question: could Zn^{2+} be incorporated into the layered $VOPO_4{\cdot}nH_2O$ framework to form a phase for zinc-ion storage?

Motivated by this consideration, herein, we report a layered phosphate, $Zn_{0.4}VOPO_4{\cdot}0.8H_2O$, by topochemical incorporation of zinc ions into the $VOPO_4{\cdot}2H_2O$ framework. The incorporation of zinc ions makes no change in the in-plane atomic arrangement and coordination environment. The resulting $Zn_{0.4}VOPO_4{\cdot}0.8H_2O$ depicted a specific capacity of 161.4 $mAh{\cdot}g^{-1}$, a discharge plateau of 1.45 V, and excellent cycling stability over 1000 cycles. The energy density of our $Zn//Zn_{0.4}VOPO_4{\cdot}0.8H_2O$ battery was as high as 219.8 $Wh{\cdot}kg^{-1}$ at a power density of 136.2 $W{\cdot}kg^{-1}$. A typical zinc ion intercalation/deintercalation mechanism has been revealed in this layered cathode. This work provides a layered hydrated phosphate as a robust cathode for ZIBs and also sheds light on modulation of multivalent-ion storage performance by a topochemical strategy in layered materials.

2. RESULTS AND DISCUSSION

A. $Zn_{0.4}VOPO_4{\cdot}0.8H_2O$ Phase. A $VOPO_4{\cdot}2H_2O$ (called as VOP) precursor was synthesized via a conventional refluxing method reported previously (Scheme 1).[21,25] A yellow precipitate was observed during the refluxing process (Figure 1a). The corresponding transmission electron microscopy (TEM) and scanning electron microscopy (SEM) characterizations demonstrate that the $VOPO_4{\cdot}2H_2O$ was crystallized in plate-like morphology with a uniform rectangular shape (Figure 1b and Figure S1). Interestingly, after solvothermal treatment of these precursor platelets in dimethoxyethane (DME) solution containing 0.5 M ZnI_2, the color of the sample changed from bright yellow into dark green (Figure 1c), suggesting the possible phase evolution and valence change of the V element during this procedure. The solvothermal condition has been optimized at 150 °C for 12 h to obtain the sample with high purity (Figure S2). The SEM and TEM images of the sample after this solvothermal treatment confirm that the rectangular morphology was well retained (Figure 1d–f). Moreover, the energy dispersive spectrum (EDS) mapping images demonstrate uniform distribution of Zn, V, O, and P elements in the platelet after the solvothermal treatment (Figure 1f). This result indicates that the Zn element has been successfully incorporated into the $VOPO_4{\cdot}2H_2O$, resulting in the formation of a Zn-rich phase. Inductively coupled plasma optical emission spectrometry analysis further confirms that the mole ratio in the Zn-rich product was 0.4:1:1 for Zn:V:P (Anal. Calcd (%): Zn, 24.1%; V, 47.2%; P, 28.7%. Found (%): Zn, 23.1%; V, 45.5%; P, 31.4%). The number (n) of coordinated water molecules was calculated to be 0.8 according to thermogravimetric analysis (TGA) (Figure S3). Accordingly, the chemical composition of the as-obtained sample can be determined as $Zn_{0.4}VOPO_4{\cdot}0.8H_2O$ (called as ZVOP). Note that the coordinated water highly decreased during the zinc ion intercalation procedure. This solvothermal reaction should be proposed as follows

$$5VOPO_4{\cdot}2H_2O + 2ZnI_2 \rightarrow 5Zn_{0.4}VOPO_4{\cdot}0.\,8H_2O + 2I_2 + 6H_2O \quad (1)$$

To better understand the chemical bonding information of this $Zn_{0.4}VOPO_4{\cdot}0.8H_2O$ phase, Raman, Fourier transform infrared spectroscopy (FTIR), and X-ray photoelectron spectroscopy (XPS) were performed subsequently. By comparing the Raman and FTIR spectra between the

Scheme 1. Schematic Illustration of the Zn^{2+} Incorporation in Layered $VOPO_4{\cdot}2H_2O$ by an Appropriate Solvothermal Process

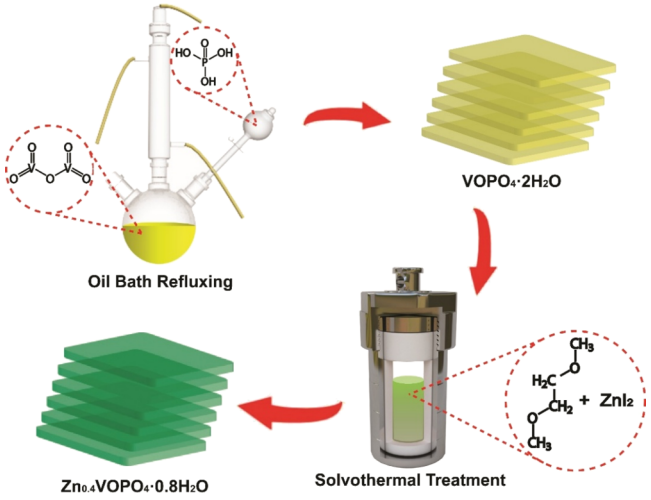

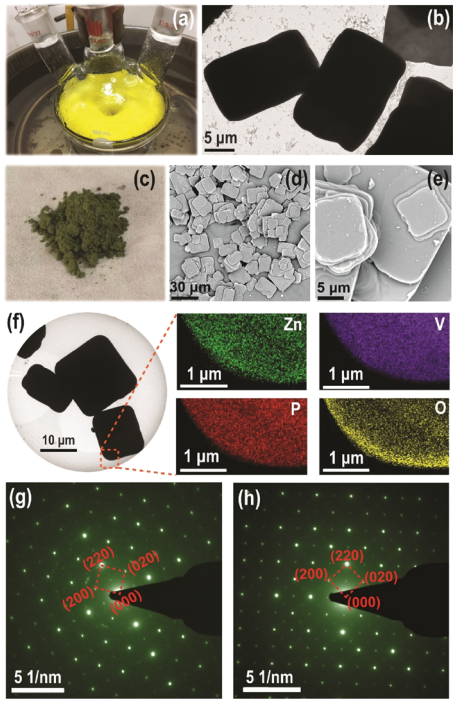

Figure 1. (a) Optical photograph for the synthesis of the $VOPO_4{\cdot}2H_2O$ precursor. (b) Typical TEM image of VOP platelets. (c) Resulting green $Zn_{0.4}VOPO_4{\cdot}0.8H_2O$ powder sample. (d, e) Characteristic SEM images. (f) TEM image and EDS mappings of $Zn_{0.4}VOPO_4{\cdot}0.8H_2O$. In-plane SAED patterns of (g) $VOPO_4{\cdot}2H_2O$ and (h) $Zn_{0.4}VOPO_4{\cdot}0.8H_2O$ platelets. (g) In-plane atomic configuration of the $Zn_{0.4}VOPO_4{\cdot}0.8H_2O$ crystal along the c axis. (h) X-ray diffraction (XRD) patterns of $VOPO_4{\cdot}2H_2O$ and $Zn_{0.4}VOPO_4{\cdot}0.8H_2O$.

https://dx.doi.org/10.1021/acsaem.0c00318
ACS Appl. Energy Mater. 2020, 3, 3919−3927

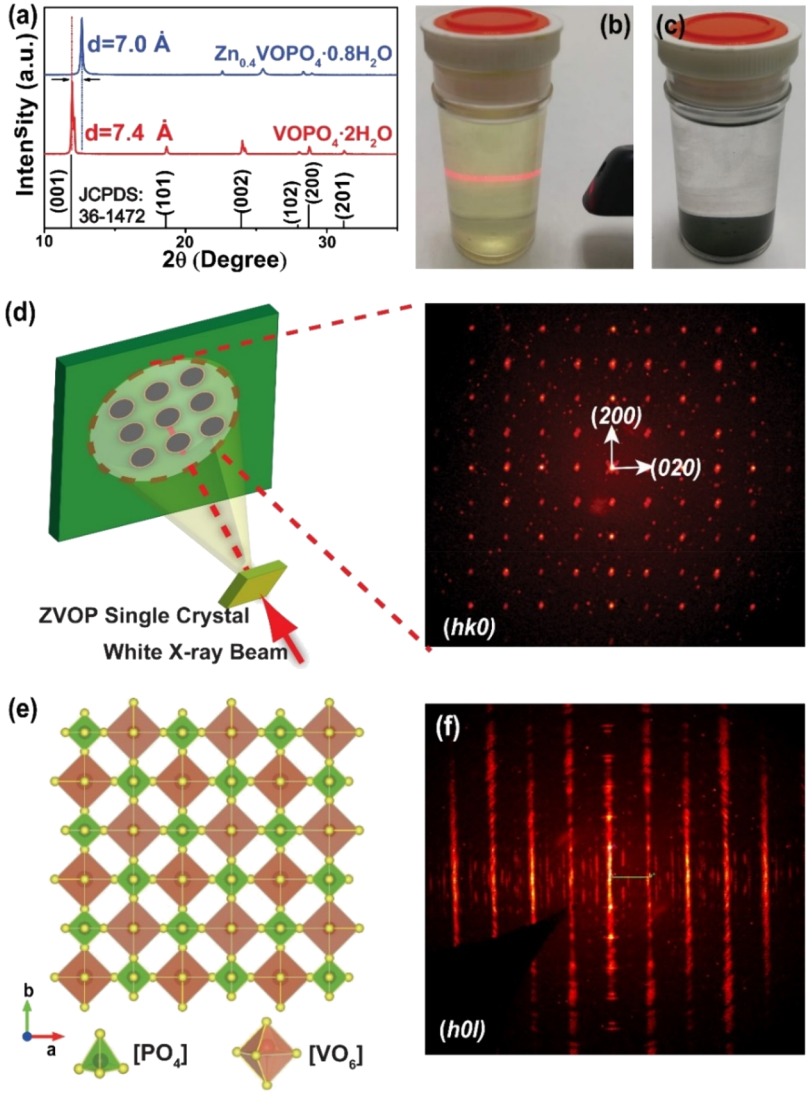

Figure 2. (a) XRD patterns of $VOPO_4·2H_2O$ and the $Zn_{0.4}VOPO_4·0.8H_2O$ powder sample. (b) Tyndall scattering effect in VOP nanosheet colloidal suspension and (c) the sedimentation of the $Zn_{0.4}VOPO_4·0.8H_2O$ bulk in isopropanol. (d) Schematic of $Zn_{0.4}VOPO_4·0.8H_2O$ single crystal diffraction and the corresponding SXRD pattern along the *c* axis. (e) SXRD pattern of the $Zn_{0.4}VOPO_4·0.8H_2O$ single crystal along the *b* axis. (f) Schematic of the proposed arrangement of Zn^{2+} sites in the $VOPO_4$ host layer.

$VOPO_4·2H_2O$ precursor and $Zn_{0.4}VOPO_4·0.8H_2O$ product (Figures S4 and S5), one can see that the hydrogen bond interaction between the H_2O molecules and the PO_4^{3-} group was weakened in $Zn_{0.4}VOPO_4·0.8H_2O$, inducing the mitigation of the steric hindrance of O−P−O stretching vibration. Accordingly, a shift to the lower wavenumber of the symmetric O−P−O stretching modes has been observed,[21,26,27] and the relatively broader and weaker band of $Zn_{0.4}VOPO_4·0.8H_2O$ compared to VOP phase suggested a lower water content.[28] From the V 2p XPS, two split peaks among the V $2p_{3/2}$ region of $Zn_{0.4}VOPO_4·0.8H_2O$ located at 518.3 and 517.1 eV assigned to V^{5+} and V^{4+} have been detected, respectively. This observation demonstrated the presence of V^{4+} after solvothermal treatment (Figure S6). The peak area ratio of V^{5+}/V^{4+} can be estimated as 0.24, which is well consistent with the stoichiometric value (0.25) in $Zn_{0.4}VOPO_4·0.8H_2O$.

We then tried to determine the crystal structure of this $Zn_{0.4}VOPO_4·0.8H_2O$ phase. Figure 1g,h depicts the in-plane selected area electron diffraction (SAED) pattern taken from an individual platelet along the *c* axis of $VOPO_4·2H_2O$ and $Zn_{0.4}VOPO_4·0.8H_2O$ platelet, respectively. Both samples exhibited typical cubic diffraction spots with the [001] zone axis, demonstrating the single-crystal nature of an individual platelet. More importantly, the in-plane lattice parameters were estimated from these SAED patterns as follows: $a = b = 6.22$ Å ($VOPO_4·2H_2O$) and $a = 6.21$ Å, $b = 6.23$ Å ($Zn_{0.4}VOPO_4·0.8H_2O$), indicating the apparent similarity on the in-plane lattice size after Zn^{2+} incorporation. From these results, we could propose that Zn^{2+} has been intercalated only into the interlayer gallery of the $VOPO_4·2H_2O$ crystal with no change in the in-plane atomic arrangement and coordination environment. In general, a topochemical reaction can be defined as adding, extracting, or substituting elements from precursors for synthesis of new materials, which retain the structure or morphology of precursors.[29] Accordingly, our strategy for the $Zn_{0.4}VOPO_4·0.8H_2O$ synthesis can be considered as a topochemical route.

Figure 2a shows the laboratory XRD patterns of the samples using Cu Kα radiation (λ = 1.5405 Å) with a graphite monochromator. One can see that the (001) peak of

https://dx.doi.org/10.1021/acsaem.0c00318
ACS Appl. Energy Mater. 2020, 3, 3919−3927

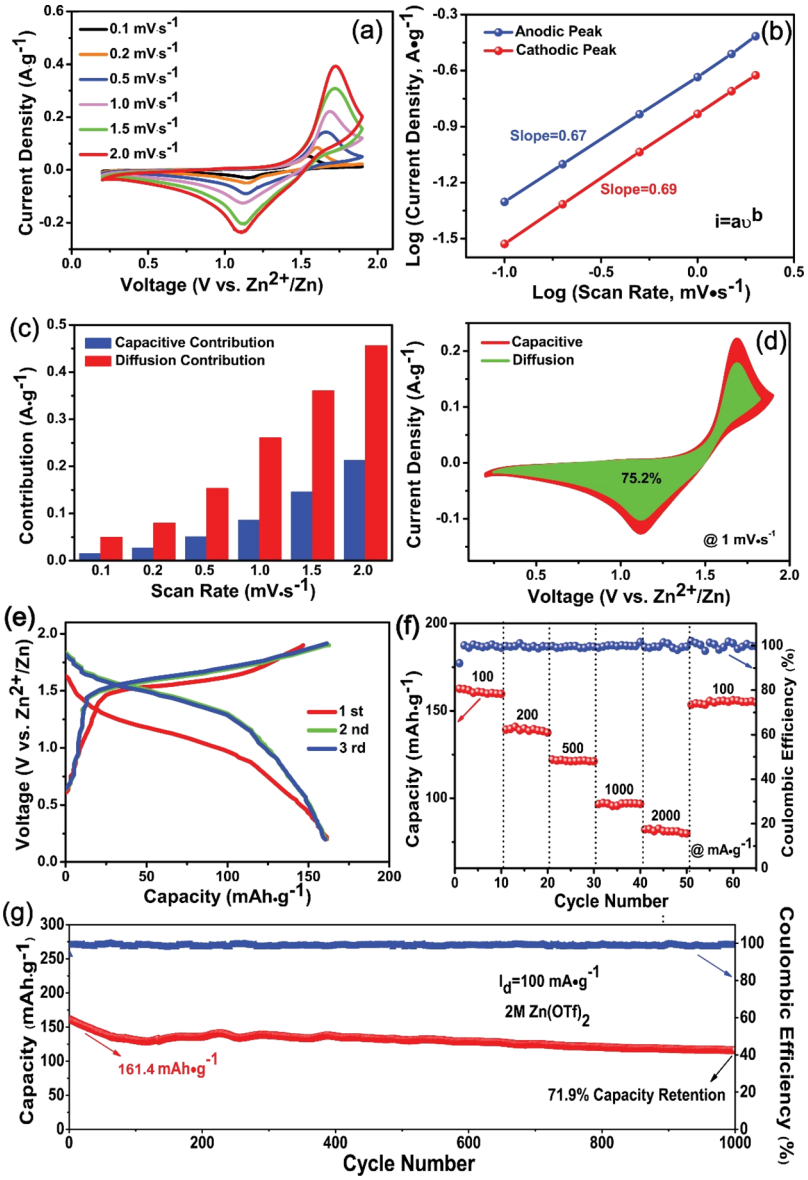

Figure 3. (a) Cyclic voltammetry (CV) curves of the $Zn_{0.4}VOPO_4{\cdot}0.8H_2O$-based battery at different scan rates. (b) Logarithm dependence of peak current density and scan rate of the ZVOP-based ZIB in the CV test. (c) Capacitive and diffusion effect contribution ratios at different CV scan rates. (d) CV curve containing the schematic of the capacitive and diffusion effect contribution at a scan rate of 1.0 $mV{\cdot}s^{-1}$. (e) Charge−discharge curves of the battery at a current density of 100 $mAh{\cdot}g^{-1}$ at first, second, and third cycles. (f) Rate capacity at current densities of 100, 200, 500, 1000, and 2000 $mA{\cdot}g^{-1}$. (g) Long-term cycle stability of $VOPO_4{\cdot}2H_2O$ and $Zn_{0.4}VOPO_4{\cdot}0.8H_2O$ cathodes at a current density of 100 $mA{\cdot}g^{-1}$.

$Zn_{0.4}VOPO_4{\cdot}0.8H_2O$ shifted to a higher degree of 12.7° compared with that of the VOP precursor, indicating a smaller interlayer *d*-spacing of 7.0 Å. A similar phenomenon has also been reported recently in Niu's work, and this reduction in *d*-spacing should result from the strong electrostatic attraction between the inserted Zn^{2+} ions and oxygen in the $[VOPO_4]$ host layer.[17] The increased electrostatic attraction has also been confirmed by the distinctive liquid exfoliation behavior between $VOPO_4{\cdot}2H_2O$ and $Zn_{0.4}VOPO_4{\cdot}0.8H_2O$. The $VOPO_4{\cdot}2H_2O$ powder can be well dispersed in isopropanol, and after a moderate ultrasonic treatment, uniform colloidal suspension was easily formed due to exfoliation of the layered bulk (Figure 2b).[21] However, the colloidal solution cannot be observed in the $Zn_{0.4}VOPO_4{\cdot}0.8H_2O$ bulk by the same treatment (Figure 2c). The absence of liquid exfoliation behavior of the $Zn_{0.4}VOPO_4{\cdot}0.8H_2O$ phase indicated much a larger bonding force between the adjacent host layers in the $Zn_{0.4}VOPO_4{\cdot}0.8H_2O$ crystal. We further performed single-crystal XRD (SXRD) characterization via synchrotron to deeply identify the crystallographic information. The reconstructed (*hk*0) section from the SXRD data showed a sharp cubic pattern (Figure 2d), which was well consistent with the SAED pattern in Figure 1h, demonstrating the unchanged $VOPO_4$ framework among the layer compared to that of VOP (Figure 2e). Nevertheless, the reconstructed (*h*0*l*) and (0*kl*) sections showed apparent streaking patterns, suggesting the presence of a large number of stacking faults parallel to the (*hk*0) plane in the present $Zn_{0.4}VOPO_4{\cdot}0.8H_2O$ crystal. More than 10 measured single crystals showed similar results (Figure 2f and Figure S7). Furthermore, the synchrotron X-ray powder diffraction (XRPD) also showed the splitting of the (001) peak into three subpeaks between 6.8 and 7.2 Å (Figure S8). This

https://dx.doi.org/10.1021/acsaem.0c00318
ACS Appl. Energy Mater. 2020, 3, 3919−3927

result also implied the uniformed interlayer distance and an unstable layered stacking of our $Zn_{0.4}VOPO_4{\cdot}0.8H_2O$. Unfortunately, the refinement of SXRD data was unsuccessful due to the presence of a large amount of stacking faults in the $Zn_{0.4}VOPO_4{\cdot}0.8H_2O$ crystal, and it is still difficult to clearly know the crystal structure and the accurate Zn^{2+} occupancy in $Zn_{0.4}VOPO_4{\cdot}0.8H_2O$.

2.2. Stable Zn//$Zn_{0.4}VOPO_4{\cdot}0.8H_2O$ Aqueous Battery. CR-2032 coin cells were assembled employing active $Zn_{0.4}VOPO_4{\cdot}0.8H_2O$ as the cathode (mass loading: 2 mg·cm^{-2}), zinc foil as the anode, glass fiber as the separator, and 2 M $Zn(CF_3SO_3)_2$ aqueous solution as the electrolyte. The CV curves of the resulting battery at various scan rates from 0.1 to 2.0 mV·s^{-1} exhibited distinct oxidation peaks and corresponding reduction peaks located between 1.5 and 1.7V and 1.1 and 1.2 V, revealing the typical electron transfer process within a wide voltage window (0.2−1.9 V) (Figure 3a). From the dependence of log(i_d) and log(v) of all the scan rates (Figure 3b), the contribution rates of the capacitive effect were calculated to be 21.7, 22.4, 23.8, 24.8, 28.7, and 31.5% at the scan rates of 0.1, 0.2, 0.5, 1.0, 1.5, and 2.0 mV·s^{-1}, respectively (Figure 3c,d). Although the major capacity contribution during the variation of the scan rate was always the battery-type effect, a gradual increase in the capacitive effect was observed with the increase in the scan rate, which should be attributed to the typical 2D morphology of our sample. Such a capacity contribution was also detected in the VOP precursor electrode at different scan rates as well (Figure S9).

The galvanostatic charge−discharge (GCD) curves (Figure 3e) for the initial cycles of the battery suggested an activation process in the first cycle, which is attributed to the initial irreversible cycle as well as the electrochemical activation process of the cathode.[24] Although the discharge plateau is lower than some other phosphate cathodes such as $LiVPO_4F$ (1.9 V)[30,31] recently reported, it is still higher than most of the traditional cathode materials including $VOPO_4{\cdot}2H_2O$ (1.15 V) (Figure S10), $Na_3V_2(PO_4)_3$ (1.1 V),[13] $LiV_2(PO_4)_3$ (1.3 V),[14] vanadium oxides and derivatives (around 0.75 V),[32−36,10] and manganese oxides (around 1.25 V).[3,37−39] The high potential should be ascribed to the "inductive effect" of strong P−O covalent bonds that drive the electron density away from the V center in the V−O−P layers, thus weakening the covalence of the V−O bonds.[26,40] As a result, the lower covalency of the V−O bonds led to the higher potential of $Zn_{0.4}VOPO_4{\cdot}0.8H_2O$.[26] The $Zn_{0.4}VOPO_4{\cdot}0.8H_2O$ cathode exhibited high specific capacities of 161.4, 140.9, 122.3, 97.1, and 82.6 mAh·g^{-1} at the current densities of 100, 200, 500, 1000, and 2000 mA·g^{-1} and recovered to 156.1 mAh·g^{-1} when the current density returned back to 100 mA·g^{-1} (Figure 3f and Figures S11 and 12). Long-term cycling stability was further studied based on different salt electrolytes at a current density of 100 mA·g^{-1} (Figure S13), demonstrating the optimal performance by choosing $Zn(CF_3SO_3)_2$ aqueous solution as the electrolyte. Remarkably, the as-constructed $Zn_{0.4}VOPO_4{\cdot}0.8H_2O$-based ZIBs exhibited excellent cycle stability with a 71.4% capacity retention after 1000 cycles with a first-cycle Coulombic efficiency of 90.7% (Figure 3g and Figures S14 and 15). The energy density of our Zn//$Zn_{0.4}VOPO_4{\cdot}0.8H_2O$ battery is 219.8 Wh·kg^{-1} at a power density of 136.2 W·kg^{-1}, which significantly surpassed those of Prussian Blue,[11,12] VS_2,[10] todorokite,[41] zinc manganate spinel, metal ion-doped manganese oxides,[42,43] and NASICON[13] counterparts recently reported. The superiority in high discharge platform and energy density of our $Zn_{0.4}VOPO_4{\cdot}0.8H_2O$ is summarized in Figure 4a,b, respectively.

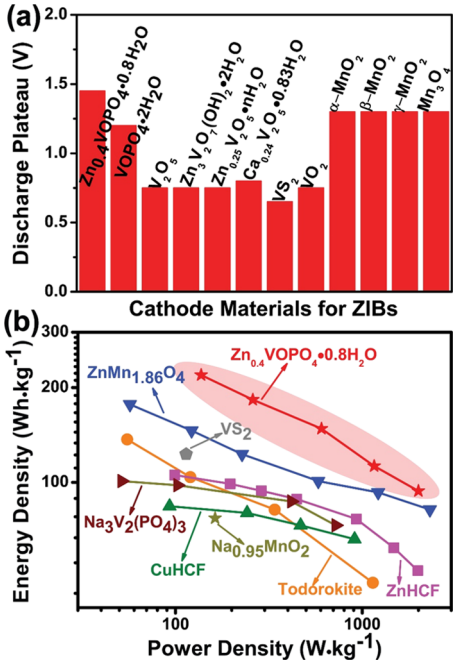

Figure 4. (a) Comparison of the discharge platform between our work and typical cathode materials of aqueous ZIBs previously reported.[3,10,13,14,32−39] (b) Ragone plot of the $Zn_{0.4}VOPO_4{\cdot}0.8H_2O$-based ZIB compared to other ZIBs based on conventional cathodes.[10−13,41−43]

To clarify the zinc ion storage mechanism of our $Zn_{0.4}VOPO_4{\cdot}0.8H_2O$, we performed *ex situ* XRD to reveal the phase evolution during the GCD procedure (Figure 5a,b). It is noteworthy that the position of the (001) peak was located at 13.5° with a *d*-spacing of 6.5 Å after the first discharge stage to a low potential of 0.2 V, which was slightly smaller than that (7.0 Å) of the pristine $Zn_{0.4}VOPO_4{\cdot}0.8H_2O$ phase in Figure 2a. During the second charge process, the location of the (001) peak gradually shifted to lower 2θ and eventually located at 12.3° at the end of a charging potential of 1.9 V (from A to E), indicating an increased interlayer spacing from 6.5 to 7.2 Å caused by Zn^{2+} deintercalation. During the second discharge process (from E to J), this peak gradually shifted back to a higher degree accompanied by the Zn^{2+} intercalation into the layered structure. At the end of the discharge process at 0.2 V, the *d*-spacing of the (001) diffraction (6.5 Å) was well consistent with the initial one (point A).The decrease in the interlayer distance after Zn^{2+} intercalation should be attributed to the enhanced electrostatic attraction between Zn^{2+} and oxygen in the layers, as reported previously.[16] In addition, according to *ex situ* XPS result of V in the completed second GCD cycle (Figure S16), the characteristic position of the V 2p peak gradually shifted to a high value of the binding energy in the charge process. It shifted back to the initial value with high reversibility in the discharge stage, corresponding to the oxidation/reduction of the V element accompanied by the deintercalation and intercalation of Zn^{2+}, respectively. This XPS result was in well agreement with the *ex situ* XRD result in the GCD procedure. The electrochemical impedance spectrum (EIS) showed two semicircles in the high-frequency area and a line in the low-frequency area

https://dx.doi.org/10.1021/acsaem.0c00318
ACS Appl. Energy Mater. 2020, 3, 3919−3927

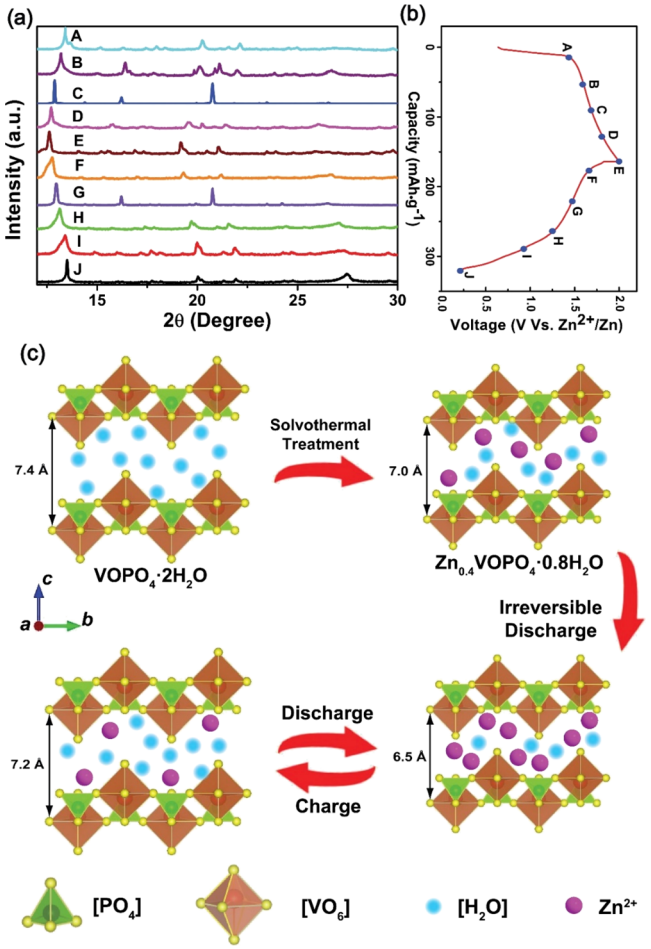

Figure 5. (a) XRD patterns of the cathode at different voltages in the second GCD cycle. (b) Corresponding GCD curve and the selected voltage points. (c) Schematic illustration of the topochemical transformation and the interlayer *d*-spacing evolution of the layered phosphate during the solvothermal treatment and charge/discharge process.

(Figure S17), indicating a diffusion-controlled battery-type mechanism of the $Zn_{0.4}VOPO_4{\cdot}0.8H_2O$ cathode,[44,45] well consistent with the zinc ion intercalation/deintercalation process demonstrated above. Therefore, the abovementioned *ex situ* XRD and XPS patterns suggest the Zn^{2+} intercalation/deintercalation mechanism of the layered $Zn_{0.4}VOPO_4{\cdot}0.8H_2O$ cathode as follows[34] (Figure 5c)

$$Zn_{0.4}VOPO_4{\cdot}nH_2O + 0.48Zn^{2+} + 0.96\ e^- \leftrightarrow Zn_{0.88}VOPO_4{\cdot}mH_2O \quad (2)$$

2.3. Wearable, Solid-State Zn//$Zn_{0.4}VOPO_4{\cdot}0.8H_2O$ Batteries. Finally, we successfully constructed a flexible, solid-state ZIB based on the ZVOP cathode and broaden its application potential in the wearable electronic field. Figure 6a shows the sandwich structure of the as-fabricated device, which was assembled employing ZVOP@CFC as the cathode (loading mass: 2 $mg{\cdot}cm^{-2}$), Zn@CFC as the anode, $Zn(ClO_4)_2$@PVA as the solid-state electrolyte, and facile filter paper as the separator. Notably, $Zn(ClO_4)_2$ employed here served as the electrolyte salt due to the higher solubility of the salt than those of $Zn(CF_3SO_3)_2$ and $ZnSO_4$ in PVA aqueous solution. The SEM image of the Zn@CFC anode (Figure 6b) demonstrated that the CFC surface was densely covered by the electrodeposited Zn thin layer. The GCD curves of the single device and two devices in series both exhibited a steady charge and discharge platform in the operation windows of 0.2 to 1.9 V and 0.4 to 3.8 V, respectively (Figure 6c). Two assembled and fully charged flexible ZIBs could easily drive a group of LEDs in series (Figure 6d). Two pieces of the devices were equipped on the glove after full charging. With the bending angle of the devices changing from 0° to 45°, 90°, and returned back to the normal state, a group of LEDs can be illuminated continuously without flicker (Figure 6e–h), demonstrating the outstanding flexibility of our devices and potential applications in the wearable electronics.

3. CONCLUSIONS

In summary, we demonstrated a layered $Zn_{0.4}VOPO_4{\cdot}0.8H_2O$ synthesized topochemically by incorporation of zinc ions into the $VOPO_4{\cdot}2H_2O$ framework as a robust cathode material for rechargeable ZIBs. The incorporation of zinc ions makes no change in the in-plane atomic arrangement and coordination environment. This layered compound combines both high discharge voltage (1.45 V) and excellent cycling stability (over 1000 cycles). The energy density of our Zn//$Zn_{0.4}VOPO_4{\cdot}0.8H_2O$ battery was as high as 219.8 $Wh{\cdot}kg^{-1}$ at a power density of 136.2 $W{\cdot}kg^{-1}$, surpassing those of Prussian Blue, VS_2, todorokite, metal ion-doped manganese oxides, and NASICON counterparts recently reported. A typical intercalation/deintercalation storage mechanism has been revealed in this layered compound. Our work opened up a new avenue on the modulation of multivalent-ion storage performance by a topochemical strategy in layered compounds. In the next work, we will continue to optimize the battery behavior by carefully controlling Zn/V atomic ratios in this layered phosphate series.

4. EXPERIMENTAL SECTION

4.1. Material Synthesis. The precursor $VOPO_4{\cdot}2H_2O$ (VOP) was synthesized according to a convenient oil bath refluxing method reported in the early literature. In the typical procedure, 4.8 g of V_2O_5, 26.6 mL of H_3PO_4, and 115.4 mL of DI water were added into a three-necked flask, followed by a short-time magnetic stirring and then heating at 110 °C in the oil bath with reflux condensation. After the reaction system was cooled down to room temperature naturally, the yellow precipitate was collected by centrifugation and washed with DI water and acetone three times. The resulting sample was dried at 60 °C in a vacuum oven so as to obtain $VOPO_4{\cdot}2H_2O$. Then, 0.3 g of oven-dried $VOPO_4{\cdot}2H_2O$ and 5.8 g of ZnI_2 were added into 60 mL of DME, and the mixture was kept under stirring for 30 min to form a homogeneous yellow-green solution. The mixture was then transferred into a 100 mL Teflon-lined strainless steel autoclave and kept at 150 °C for 12 h in the oven. The dark-green precipitate at the bottom of the reactor was collected by filtration and washed with DME several times. The sample was then dried in a vacuum oven at 60 °C for 8 h to obtain the $Zn_{0.4}VOPO_4{\cdot}0.8H_2O$ (ZVOP) product. For the liquid exfoliation experiment, 30 mg of the powder sample (ZVOP or VOP bulk) was dispersed in 20 mL of isopropanol solvent, followed by a moderate ultrasonication treatment for 30 min.

4.2. Material Characterization. The structure morphology and structure characterization were characterized by SEM (Phenom Pro X), high-resolution TEM, and laboratory XRD (Bruker D8-A25 diffractometer using Cu Kα radiation (λ = 1.5406 Å)). The SAED and EDS mapping were carried out during the TEM measurement (Philips CM 200 FEG field emission microscope) process to gather detailed information of the phase structure and chemical element distribution of the sample. Further information of the chemical bonding condition and the microscopic was recorded by means of XPS (PHI 5000C EACA), Raman spectroscopy (RENISHAW inVia),

https://dx.doi.org/10.1021/acsaem.0c00318
ACS Appl. Energy Mater. 2020, 3, 3919–3927

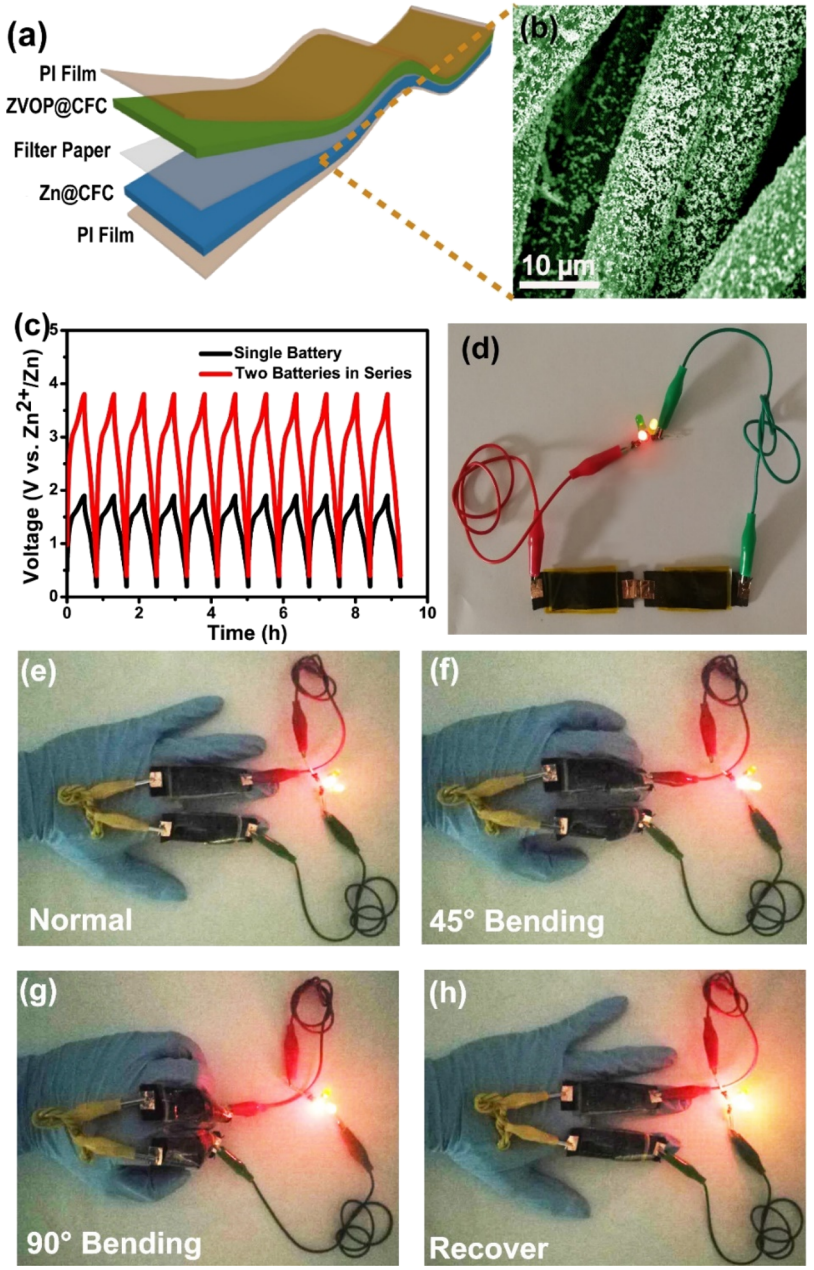

Figure 6. (a) Sandwich structure of the flexible battery. (b) SEM image of the carbon fiber cloth undergoing zinc electrodeposition. (c) Dependence of voltage and time of single battery/batteries in series during the charge and discharge procedures. (d) Photograph of a group LEDs driven by two fully charged batteries in series. (e–h) Exhibition of the stable output performance of the flexible batteries with different bending angles.

FTIR (Bruker Tensor II), TGA (SDT Q600), and inductively coupled plasma atomic emission spectrometry (PerkinElmer Optima 8000). Synchrotron XRPD and SXRD data were collected at PD and MX2 beamlines, Australian Synchrotron (ANSTO), respectively. For the *ex situ* XRD characterization, the ZVOP-based battery was first discharged to the lower limit of the voltage (0.2 V) with a complete Zn^{2+} intercalation procedure, and we then carried out the *ex situ* XRD characterization in the second GCD cycle.

4.3. Electrochemical Measurement. The ZVOP electrode was prepared by mixing ZVOP, acetylene black, and poly(vinylidene difluoride) on the basis of a mass ratio of 7:2:1 with the moderate addition of 1-methyl-2-pyrrolidinone; then, the uniform slurry was coated onto a piece of 304 stainless steel foil and dried at 80 °C for 10 h in a vacuum oven. The slurry-coated foil cut into Φ10 mm electrodes served as the cathode (mass loading: 2 mg·cm^{-2}), while the zinc foil washed with ethanol and the glass fiber membrane were used as the anode and separator, respectively, and 2 M $Zn(CF_3SO_3)_2$ (2 M $ZnSO_4$, 2 M $Zn(ClO_4)_2$) aqueous solution was prepared as the electrolyte. The CR-2032 cell was assembled in air using the beforehand electrodes and other relevant components. A LAND battery test system (CT2001A) was employed to evaluate the electrochemical performance of the battery. The CV test and EIS with a frequency range from 1 MHz to 0.1 Hz and an applied AC of 5 mV were performed on the electrochemical workstation (CHI660E). The similar method was also applied to the preparation and evaluation of the VOP-based ZIB.

4.4. Fabrication and Functional Test of the Flexible All-Solid-State Battery. A quasi solid flexible zinc-ion battery was fabricated using the aforementioned slurry-coated carbon fiber cloth (CFC) as the cathode (mass loading: 2 mg·cm^{-2}), CFC with a layer of zinc electrodeposited coating as the anode, a piece of filter paper as the separator, and 2 M $Zn(ClO_4)_2$@poly(vinyl alcohol) (PVA) as the

https://dx.doi.org/10.1021/acsaem.0c00318
ACS Appl. Energy Mater. 2020, 3, 3919–3927

electrolyte. The electrolyte was prepared by adding 3 g of PVA to 30 mL of 2 M $Zn(ClO_4)_2$ aqueous solution little by little with continuous stirring, followed by oil bath treatment at 80 °C for 2 h and gathering of the thick sample when it cooled down to room temperature. The electrochemical deposition of the zinc layer on the CFC was executed on CHI660E using a potentiostatic model at −0.7 V (vs Zn^{2+}/Zn) for 2000 s. The ultimate flexible all-solid-state battery was assembled and sealed with the polyimide (PI) film to form a stable sandwich structure.

4.5. Calculation Methods. From the dependence of $\log(i_d)$ and $\log(v)$ of all the scan rates (Figure S10), the capacity contributed by the capacitive effect and battery-type effect (diffusion effect) can be clearly distinguished by the following equations[46,47]

$$I_p = av^b \tag{3}$$

$$I_p = C_1 v + C_2 v^{1/2} \tag{4}$$

where I_p ($A \cdot g^{-1}$) is the peak current density at different scan rates, v is the corresponding scan rates varied from 0.1 to 2 $mV \cdot s^{-1}$, a and b are adjustable values due to the kinetic process, C_1 and C_2 are the constant factors of the capacity contribution of the surface pseudocapacitive effect and battery-type effect, respectively.

With a deformation of the above equation, the specific contribution rate of different internal mechanisms can be solved according to the following equation

$$\frac{I_p}{v^{1/2}} = C_1 v^{1/2} + C_2 \tag{5}$$

The specific energy density ($Wh \cdot kg^{-1}$) and average specific power density ($W \cdot kg^{-1}$) of the ZVOP- and VOP-based batteries were calculated in terms of the following equations

$$E_s = \int_{V_0}^{V_1} C_s(V) \tag{6}$$

$$P_s = \frac{E_s}{t} \tag{7}$$

where E_s is the calculated specific energy density ($Wh \cdot kg^{-1}$), P_s is the average specific power density ($W \cdot kg^{-1}$), C_s ($mAh \cdot g^{-1}$) is the specific capacity of the battery, V_0 and V_1 is the voltage lower limit and voltage upper limit of the discharge procedure, respectively, and t is the discharge time (h). All of the properties including specific capacity, energy density, and power density are calculated based on the mass loading of the active material (ZVOP or VOP) in the coated slurry on the substrate.

■ ASSOCIATED CONTENT

Supporting Information

The Supporting Information is available free of charge at https://pubs.acs.org/doi/10.1021/acsaem.0c00318.

Supplementary characterizations; analysis for ZVOP including SEM, TGA, Raman, FTIR, and XPS; and a series of electrochemical performance (Figures S1−S19) (PDF)

■ AUTHOR INFORMATION

Corresponding Author

Linfeng Hu − *Department of Materials Science, Fudan University, Shanghai 200433, P. R. China;* orcid.org/0000-0002-0640-508X; Email: linfenghu@fudan.edu.cn

Authors

Zeyi Wu − *Department of Materials Science, Fudan University, Shanghai 200433, P. R. China*

Yanan Wang − *Department of Materials Science, Fudan University, Shanghai 200433, P. R. China*

Lin Zhang − *Department of Materials Science, Fudan University, Shanghai 200433, P. R. China*

Le Jiang − *Department of Materials Science, Fudan University, Shanghai 200433, P. R. China*

Wenchao Tian − *Department of Materials Science, Fudan University, Shanghai 200433, P. R. China*

Cailing Cai − *Department of Materials Science, Fudan University, Shanghai 200433, P. R. China*

Jason Price − *Australian Synchrotron (ANSTO), Clayton 3168, Australia*

Qinfen Gu − *Australian Synchrotron (ANSTO), Clayton 3168, Australia;* orcid.org/0000-0001-9209-4208

Complete contact information is available at: https://pubs.acs.org/10.1021/acsaem.0c00318

Notes

The authors declare no competing financial interest.

■ ACKNOWLEDGMENTS

This work was financially supported by the National Natural Science Foundation of China (nos. 51872051 and 51701042), the Science and Technology Committee of Shanghai Municipality (18520723100), and the Researching Program of State Grid Corporation of China (GYW17201800011). Part of the experiment was performed on PD and MX2 beamlines at Australian Synchrotron (ANSTO).

■ REFERENCES

(1) Wang, F.; Borodin, O.; Gao, T.; Fan, X.; Sun, W.; Han, F.; Faraone, A.; Dura, J. A.; Xu, K.; Wang, C. Highly Reversible Zinc Metal Anode for Aqueous Batteries. *Nat. Mater.* **2018**, *17*, 543−549.

(2) Song, M.; Tan, H.; Chao, D.; Fan, H. J. Recent Advances in Zn-Ion Batteries. *Adv. Funct. Mater.* **2018**, *28*, 1802564.

(3) Pan, H.; Shao, Y.; Yan, P.; Cheng, Y.; Han, K. S.; Nie, Z.; Wang, C.; Yang, J.; Li, X.; Bhattacharya, P.; Mueller, K. T.; Liu, J. Reversible Aqueous Zinc/Manganese Oxide Energy Storage from Conversion Reactions. *Nat. Energy* **2016**, *1*, 16039.

(4) Li, C.; Xie, X.; Liang, S.; Zhou, J. Issues and Future Perspective on Zinc Metal Anode for Rechargeable Aqueous Zinc-ion Batteries. *Energy Environ. Mater.* **2020**, DOI: 10.1002/eem2.12067.

(5) Guo, X.; Zhou, J.; Bai, C.; Li, X.; Fang, G.; Liang, S. Zn/MnO_2 Battery Chemistry with Dissolution-Deposition Mechanism. *Mater. Today Energy* **2020**, *16*, 100396.

(6) Li, H.; Han, C.; Huang, Y.; Huang, Y.; Zhu, M.; Pei, Z.; Xue, Q.; Wang, Z.; Liu, Z.; Tang, Z.; Wang, Y.; Kang, F.; Li, B.; Zhi, C. An Extremely Safe and Wearable Solid-State Zinc Ion Battery Based on a Hierarchical Structured Polymer Electrolyte. *Energy Environ. Sci.* **2018**, *11*, 941−951.

(7) Ma, L.; Chen, S.; Li, H.; Ruan, Z.; Tang, Z.; Liu, Z.; Wang, Z.; Huang, Y.; Pei, Z.; Zapien, J. A.; Zhi, C. Initiating a mild aqueous electrolyte Co_3O_4/Zn battery with 2.2 V-high voltage and 5000-cycle lifespan by a Co(iii) rich-electrode. *Energy Environ. Sci.* **2018**, *11*, 2521−2530.

(8) Yan, M.; He, P.; Chen, Y.; Wang, S.; Wei, Q.; Zhao, K.; Xu, X.; An, Q.; Shuang, Y.; Shao, Y.; Mueller, K. T.; Mai, L.; Liu, J.; Yang, J. Water-Lubricated Intercalation in $V_2O_5 \cdot nH_2O$ for High-Capacity and High-Rate Aqueous Rechargeable Zinc Batteries. *Adv. Mater.* **2018**, *30*, 1703725.

(9) Zhang, N.; Dong, Y.; Jia, M.; Bian, X.; Wang, Y.; Qiu, M.; Xu, J.; Liu, Y.; Jiao, L.; Cheng, F. Rechargeable Aqueous $Zn-V_2O_5$ Battery with High Energy Density and Long Cycle Life. *ACS Energy Lett.* **2018**, *3*, 1366−1372.

(10) He, P.; Yan, M.; Zhang, G.; Sun, R.; Chen, L.; An, Q.; Mai, L. Layered VS_2 Nanosheet-Based Aqueous Zn Ion Battery Cathode. *Adv. Energy Mater.* **2017**, *7*, 1601920.

(11) Trócoli, R.; La Mantia, F. An Aqueous Zinc-Ion Battery Based on Copper Hexacyanoferrate. *ChemSusChem* **2015**, *8*, 481−485.
(12) Zhang, L.; Chen, L.; Zhou, X.; Liu, Z. Towards High-Voltage Aqueous Metal-Ion Batteries beyond 1.5 V: the Zinc/Zinc Hexacyanoferrate system. *Adv. Energy Mater.* **2015**, *5*, 1400930.
(13) Li, G.; Yang, Z.; Jiang, Y.; Jin, C.; Huang, W.; Ding, X.; Huang, Y. Towards Polyvalent Ion Batteries: A Zinc-Ion Battery Based on NASICON Structured $Na_3V_2(PO4)_3$. *Nano Energy* **2016**, *25*, 211−217.
(14) Wang, F.; Hu, E.; Sun, W.; Gao, T.; Ji, X.; Fan, X.; Han, F.; Yang, X.-Q.; Xu, K.; Wang, C. A Rechargeable Aqueous Zn^{2+}-Battery with High Power Density and a Long Cycle-Life. *Energy Environ. Sci.* **2018**, *11*, 3168−3175.
(15) Chen, K.; Li, L. Ordered Structures with Functional Units as a Paradigm of Material Design. *Adv. Mater.* **2019**, *31*, 1901115.
(16) Wang, F.; Sun, W.; Shadike, Z.; Hu, E.; Ji, X.; Gao, T.; Yang, X.-Q.; Xu, K.; Wang, C. How Water Accelerates Bivalent Ion Diffusion at the Electrolyte/Electrode Interface. *Angew. Chem., Int. Ed.* **2018**, *57*, 11978−11981.
(17) Wan, F.; Zhang, Y.; Zhang, L.; Liu, D.; Wang, C.; Song, L.; Niu, Z.; Chen, J. Reversible Oxygen Redox Chemistry in Aqueous Zinc-Ion Batteries. *Angew. Chem., Int. Ed.* **2019**, *58*, 7062−7067.
(18) Shi, H.-Y.; Song, Y.; Qin, Z.; Li, C.; Guo, D.; Liu, X.-X.; Sun, X. Inhibiting $VOPO_4{\cdot}x\ H_2O$ Decomposition and Dissolution in Rechargeable Aqueous Zinc Batteries to Promote Voltage and Capacity Stabilities. *Angew. Chem., Int. Ed.* **2019**, *58*, 16057−16061.
(19) Nakato, T.; Furumi, Y.; Terao, N.; Okuhara, T. Reaction of Layered Vanadium Phosphorus Oxides, $VOPO_4{\cdot}2H_2O$ and $VOHPO_4{\cdot}0.5H_2O$, with Amines and Formation of Exfoliative Intercalation Compounds. *J. Mater. Chem.* **2000**, *10*, 737−743.
(20) Goubitz, K.; Čapková, P.; Melánová, K.; Molleman, W.; Schenk, H. Structure Determination of Two Intercalated Compounds $VOPO_4{\cdot}(CH_2)_4O$ and $VOPO_4{\cdot}OH\text{-}(CH_2)_2\text{-}O\text{-}(CH_2)_2\text{-}OH$; synchrotron powder diffraction and molecular modelling. *Acta Crystallogr., Sect. B: Struct. Sci.* **2001**, *57*, 178−183.
(21) Wu, C.; Lu, X.; Peng, L.; Xu, K.; Peng, X.; Huang, J.; Yu, G.; Xie, Y. Two-Dimensional Vanadyl Phosphate Ultrathin Nanosheets for High Energy Density and Flexible Pseudocapacitors. *Nat. Commun.* **2013**, *4*, 2431.
(22) He, G.; Kan, W. H.; Manthiram, A. A 3.4 V Layered $VOPO_4$ Cathode for Na-Ion Batteries. *Chem. Mater.* **2016**, *28*, 682−688.
(23) Ji, X.; Chen, J.; Wang, F.; Sun, W.; Ruan, Y.; Miao, L.; Jiang, J.; Wang, C. Water-Activated $VOPO_4$ for Magnesium Ion Batteries. *Nano Lett.* **2018**, *18*, 6441−6448.
(24) Huang, J.; Wang, Z.; Hou, M.; Dong, X.; Liu, Y.; Wang, Y.; Xia, Y. Polyaniline-Intercalated Manganese Dioxide Nanolayers as a High-Performance Cathode Material for an Aqueous Zinc-Ion Battery. *Nat. Commun.* **2018**, *9*, 2906.
(25) Dupré, N.; Gaubicher, J.; Ngenault, J.; Quarton, M. Electrochemical study of intercalated vanadyl phosphate. *J. Solid State Eletrochem.* **2004**, *8*, 322−329.
(26) Fang, Y.; Liu, Q.; Xiao, L.; Rong, Y.; Liu, Y.; Chen, Z.; Ai, X.; Cao, Y.; Yang, H.; Xie, J.; Sun, C.; Zhang, X.; Aoun, B.; Xing, X.; Xiao, X.; Ren, Y. A Fully Sodiated $NaVOPO_4$ with Layered Structure for High-Voltage and Long-Lifespan Sodium-Ion Batteries. *Chem* **2018**, *4*, 1167−1180.
(27) Beneš, L.; Melánová, K.; Trchová, M.; Čapková, P.; Matějka, P. Water/Ethanol Displacement Reactions in Vanadyl Phosphate. *Eur. J. Inorg. Chem.* **1999**, *12*, 2289−2294.
(28) Beneš, L.; Melánová, K.; Svoboda, J.; Zima, V. Intercalation Chemistry of Layered Vanadyl Phosphate: a Review. *J. Inclusion Phenom. Macrocyclic Chem.* **2012**, *73*, 33−53.
(29) Xiao, X.; Wang, H.; Urbankowski, P.; Gogotsi, Y. Topochemical Synthesis of 2D Materials. *Chem. Soc. Rev.* **2018**, *47*, 8744.
(30) Liu, Z.; Yang, Q.; Wang, D.; Liang, G.; Zhu, Y.; Mo, F.; Huang, Z.; Li, X.; Ma, L.; Tang, T.; Lu, Z.; Zhi, C. A Flexible Solid-State Aqueous Zinc Hybrid Battery with Flat and High-Voltage Discharge Plateau. *Adv. Energy Mater.* **2019**, 1902473.
(31) Yang, Q.; Liang, G.; Guo, Y.; Liu, Z.; Yan, B.; Wang, D.; Huang, Z.; Li, X.; Fan, J.; Zhi, C. Do Zinc Dendrites Exist in Neutral Zinc Batteries: A Developed Electrohealing Strategy to In Situ Rescue In-Service Batteries. *Adv. Mater.* **2019**, 1903778.
(32) Zhou, J.; Shan, L.; Wu, Z.; Guo, X.; Fang, G.; Liang, S. Investigation of V_2O_5 as a Low-Cost Rechargeable Aqueous Zinc Ion Battery Cathode. *Chem. Commun.* **2018**, *54*, 4457−4460.
(33) Xia, C.; Guo, J.; Lei, Y.; Liang, H.; Zhao, C.; Alshareef, H. N. Rechargeable Aqueous Zinc-Ion Battery Based on Porous Framework Zinc Pyrovanadate Intercalation Cathode. *Adv. Mater.* **2018**, *30*, 1705580.
(34) Kundu, D.; Adams, B. D.; Duffort, V.; Vajargah, S. H.; Nazar, L. F. A High-Capacity and Long-Life Aqueous Rechargeable Zinc Battery Using a Metal Oxide Intercalation Cathode. *Nat. Energy* **2016**, *1*, 16119.
(35) Xia, C.; Guo, J.; Li, P.; Zhang, X.; Alshareef, H. N. Highly Stable Aqueous Zinc-Ion Storage Using a Layered Calcium Vanadium Oxide Bronze Cathode. *Angew. Chem., Int. Ed.* **2018**, *57*, 3943−3948.
(36) Ding, J.; Du, Z.; Gu, L.; Li, B.; Wang, L.; Wang, S.; Gong, Y.; Yang, S. Ultrafast Zn^{2+} Intercalation and Deintercalation in Vanadium Dioxide. *Adv. Mater.* **2018**, 1800762.
(37) Zhang, N.; Cheng, F.; Liu, J.; Wang, L.; Long, X.; Liu, X.; Li, F.; Chen, J. Rechargeable Aqueous Zinc-Manganese Dioxide Batteries with High Energy and Power Densities. *Nat. Commun.* **2017**, *8*, 405.
(38) Xu, C.; Li, B.; Du, H.; Kang, F. Energetic Zinc Ion Chemistry: The Rechargeable Zinc Ion Battery. *Angew. Chem., Int. Ed.* **2012**, *51*, 933−935.
(39) Zhu, C.; Fang, G.; Zhou, J.; Guo, J.; Wang, Z.; Wang, C.; Li, J.; Tang, Y.; Liang, S. Binder-Free Stainless Steel@Mn_3O_4 Nanoflower Composite: a High-Activity Aqueous Zinc-Ion Battery Cathode with High-Capacity and Long Cycle-Life. *J. Mater. Chem. A* **2018**, *6*, 9677−9683.
(40) Sun, Y.; Wu, C.; Xie, Y. Sonochemical synthesis of nanostructured $VOPO_4{\cdot}2H_2O$/Carbon Nanotube Composites with Improved Lithium Ion Battery Performance. *J. Nanopart. Res.* **2010**, *12*, 417−427.
(41) Lee, J.; Ju, J. B.; Cho, W. I.; Cho, B. W.; Oh, S. H. Todorokite-Type MnO_2 as a Zinc-Ion Intercalating Material. *Electrochim. Acta* **2013**, *112*, 138−143.
(42) Zhang, N.; Cheng, F.; Liu, Y.; Zhao, Q.; Lei, K.; Chen, C.; Liu, X.; Chen, J. Cation-Deficient Spinel $ZnMn_2O_4$ Cathode in Zn$(CF_3SO_3)_2$ Electrolyte for Rechargeable Aqueous Zn-Ion Battery. *J. Am. Chem. Soc.* **2016**, *138*, 12894−12901.
(43) Zhang, B.; Liu, Y.; Wu, X.; Yang, Y.; Chang, Z.; Wen, Z.; Wu, Y. An Aqueous Rechargeable Battery Based on Zinc Anode and $Na_{0.95}MnO_2$. *Chem. Commun.* **2014**, *50*, 1209−1211.
(44) Wang, R.; Xu, C.; Sun, J.; Liu, Y.; Gao, L.; Yao, H.; Lin, C. Heat-Induced Formation of Porous and Free-Standing MoS_2/GS Hybrid Electrodes for Binder-Free and Ultralong-Life Lithium Ion Batteries. *Nano Energy* **2014**, *8*, 183−195.
(45) Chu, A.; Braatz, P. Comparison of Commercial Supercapacitors and High-Power Lithium-Ion Batteries for Power-Assist Applications in Hybrid Electric Vehicles I: Initial characterization. *J. Power Sources* **2002**, *112*, 236−246.
(46) Yan, Y.; Hao, B.; Wang, D.; Chen, G.; Markweg, E.; Albrecht, A.; Schaaf, P. Understanding the fast lithium storage performance of hydrogenated TiO_2 nanoparticles. *J. Mater. Chem. A* **2013**, *1*, 14507−14513.
(47) Gogotsi, Y.; Penner, R. M. Energy Storage in Nanomaterials - Capacitive, Pseudocapacitive, or Battery-like? *ACS Nano* **2018**, *12*, 2081−2083.

https://dx.doi.org/10.1021/acsaem.0c00318
ACS Appl. Energy Mater. 2020, 3, 3919−3927